Supplementary Information

Ultrahigh photoresponse in strain- and domain-engineered large-scale MoS_2 monolayer films

Ye Seul Jung[a], Jae Woo Park[a,b], Ji Yeon Kim[a], Youngseo Park[c], Dong Gue Roe[d], Junseok Heo[c], Jeong Ho Cho[e], and Yong Soo Cho[a*]

[a]Department of Materials Science and Engineering, Yonsei University, Seoul 03722, Republic of Korea
[b]Samsung Electronics Co. Ltd., Gyeonggi-do 16677, Republic of Korea
[c]Department of Electrical and Computer Engineering, Ajou University, Suwon 16499, Republic of Korea
[d]School of Electrical and Electronic Engineering, Yonsei University, Seoul 03722, Republic of Korea
[e]Department of Chemical and Biomolecular Engineering, Yonsei University, Seoul 03722, Republic of Korea

*E-mail: ycho@yonsei.ac.kr

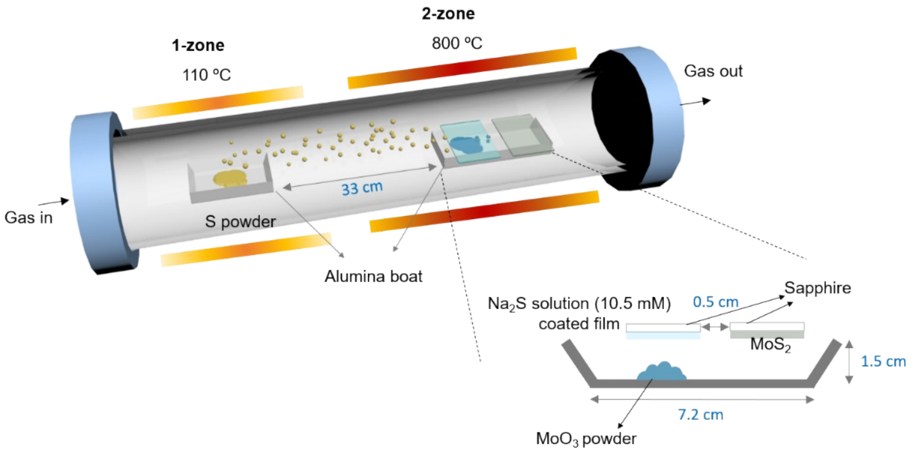

Fig. S1 Schematic illustration of the Na_2S-assisted CVD process for synthesizing monolayer MoS_2 thin films, which accommodates two heating zones for the evaporation of the sulfur source and the reaction of the TMD from a separate source of MoO_3. Detailed dimensions are provided in the cross-sectional schematic.

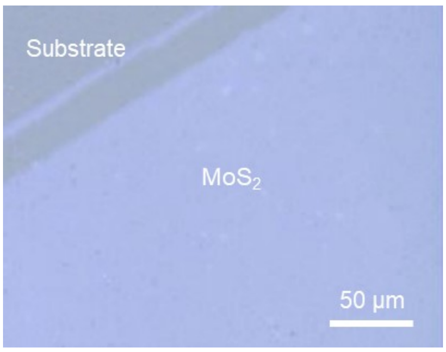

Fig. S2 Optical microscopy image near the boundary of the synthesized MoS_2 and sapphire substrate, indicating the uniform coverage of the film with no macroscale defects on the film surface.

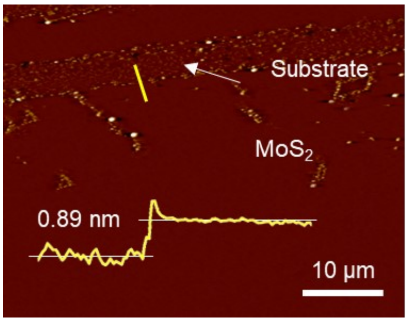

Fig. S3 AFM surface image with the line profile across the boundary between MoS_2 and substrate, indicates that the film has a smooth surface with no topographical interruptions. The line profile across the film–substrate boundary shows a step height of ~0.89 nm, indicating a monolayer.

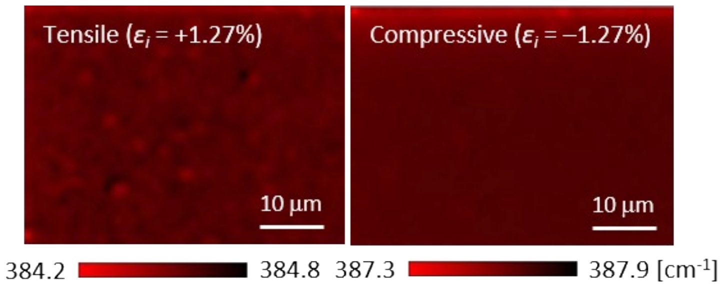

Fig. S4 Raman mapping images of the E^1_{2g} vibrational mode for the MoS_2 monolayer processed with in situ strains of +1.27% (left) and –1.27% (right) for the specific wavenumbers of 384.4 and 387.5 cm^{-1}, respectively. This map indicates that the relevant vibrational peak modes are tightly distributed at ~384.4 cm^{-1} for ε_i = +1.27% and at ~387.5 cm^{-1} for ε_i = –1.27% over the entire scanned images, the contrast uniformity of which also suggests the homogeneous monolayer coverage. The different average wavenumbers of 384.4 and 387.5 cm^{-1} imply a shift in the vibrational peak position depending on the presence of different levels of lattice strain.

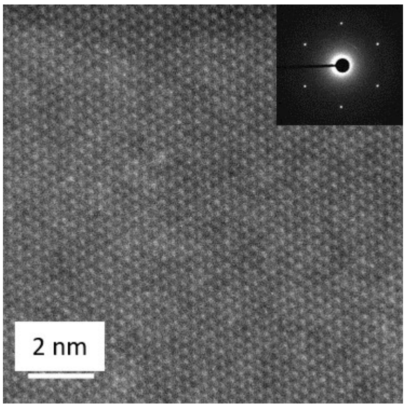

Fig. S5 HAADF-STEM image of the monolayer sample of large-scale MoS_2 monolayer film synthesized on a sapphire substrate (inset: FFT-SAED pattern).

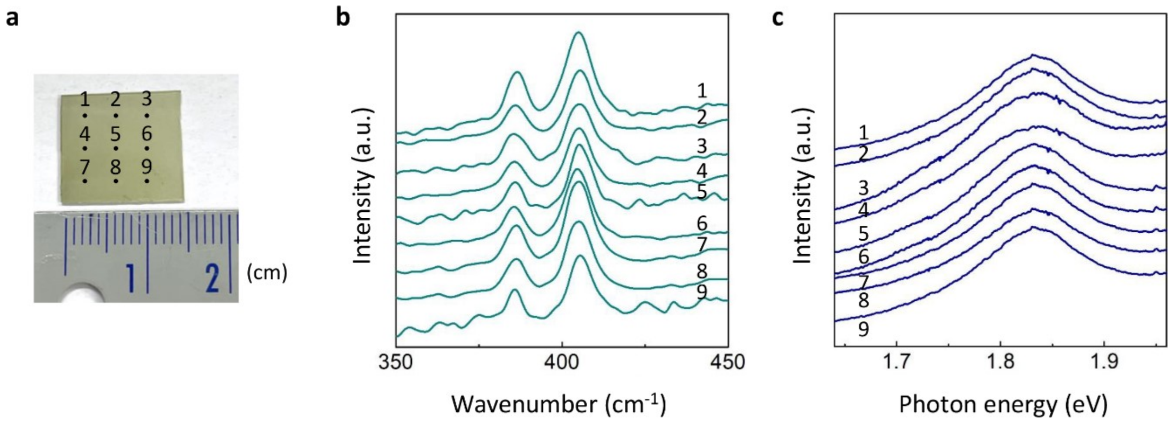

Fig. S6 (a) Photograph of a large-scale MoS_2 monolayer film synthesized on a sapphire substrate. (b) Raman spectra, and (c) PL spectra from the nine different positions in (a), indicating quite consistent spectra patterns at the different spots.

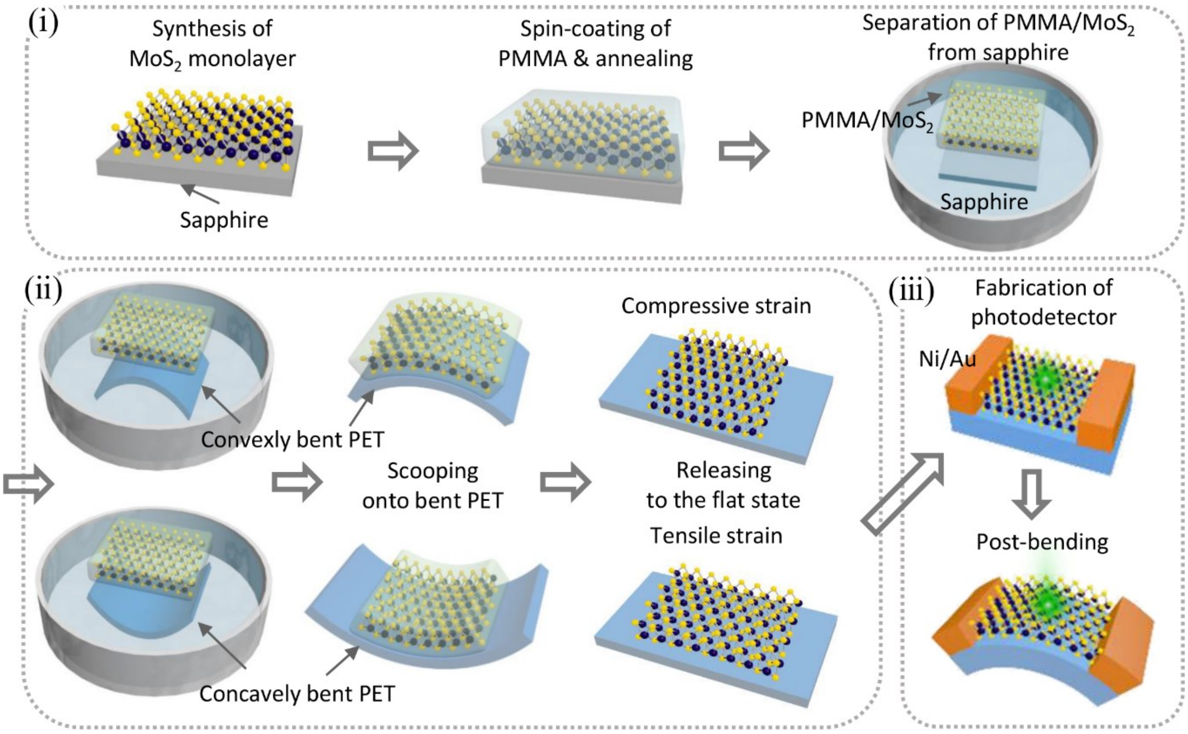

Fig. S7 Schematic illustration of the double-strain engineering of large-scale MoS_2 monolayer films: (i) the LPCVD synthesis of a large-scale MoS_2 monolayer film, (ii) transferring the MoS_2 film onto concavely or convexly pre-bent PET substrate for the first strain engineering with ±1.27% strain, and (iii) post-bending the pre-bent sample for the second strain engineering up to +2.54%.

Note: Estimation of the in situ strain

The following two steps were used to estimate the in situ bending strain applied for the monolayer MoS_2/PET sample.

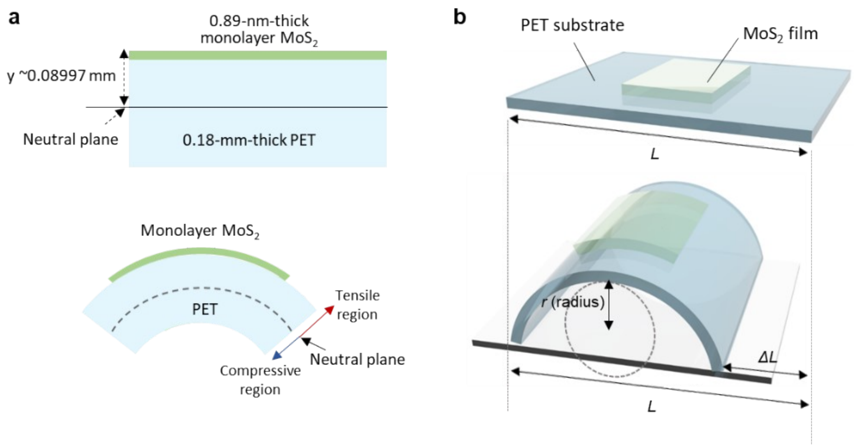

Fig. S8 (a) Schematic of the MoS2/PET structure used for the in situ process with the location of neutral plane and (b) schematic illustration of the bent substrate with defined dimensional parameters.

1) Estimation of the neutral plane

The location of the neutral plane, y, relative to the top surface was calculated for the MoS_2/PET structure by considering the contribution of each layer using the following equation reported for a multi-layered structure (*Science* **325**, 977-981 (2009)):

$$y = \frac{E^*_{MoS2} t_{MoS2}\left(t_{MoS2} - \frac{t_{MoS2}}{2}\right) + E^*_{PET} t_{PET}\left(t_{MoS2} + t_{PET} - \frac{t_{PET}}{2}\right)}{E^*_{MoS2} t_{MoS2} + E^*_{PET} t_{PET}}$$

where $E^* = E/(1\text{-}v^2)$ (here, E and v are the Young's modulus and Poisson's ratio of the layer, respectively), and t is the thickness of the layer.

The following data were used for the calculation:

$E_{MoS2} = 262$ GPa, $\nu_{MoS2} = 0.3$ for the 0.89-nm-thick MoS_2 monolayer (*2D Mater.* **1** (2014) 011007)

$E_{PET} = 3.1$ GPa, $\nu_{PET} = 0.43$ for the 0.18-mm-thick PET substrate (*Materials* **9** (2016) 850, *Rev. Sci. Instrum*. **73**, (2022) 1813)

The neutral plane y was found to be 0.08997 mm.

2) Calculation of the bending strain in the harvester

The level of strain was changed by adjusting the curvature of the loaded polymer substrate. The bending curvature radius r was calculated by the following equation (*Mater. Horiz*., **9** (2022) 1207-1215):

$$r = \frac{L}{2\pi\sqrt{\frac{\Delta L}{L} - \frac{\pi^2 t^2}{12L^2}}}$$

where L is the substrate length, ΔL is the reduced length after bending (on the bottom horizontal line) and t is the total thickness of the MoS_2 film and substrate.

The in situ strain ε_i applied in the monolayer MoS_2 layer was calculated using the relation $\varepsilon_i = (y\text{-}x)/r$, where x is the distance from the top of the photodetector to the middle of the MoS_2 layer, and r is the radius of the bending curvature. The subsequent bending strain values were finally attained with respect to the magnitude of the bending curvature. As a result, the bending with the radius of curvatures of 37.0, 17.4, 10.0 and 7.1 mm were estimated to create the in situ strains of 0.24, 0.52, 0.90 and 1.27%, respectively.

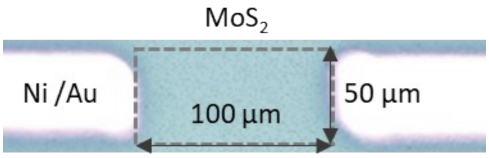

Fig. S9 Optical image of the channel between the Ni/Au electrodes in a monolayer MoS_2 photodetector, showing an active area of ~100 µm × ~50 µm.

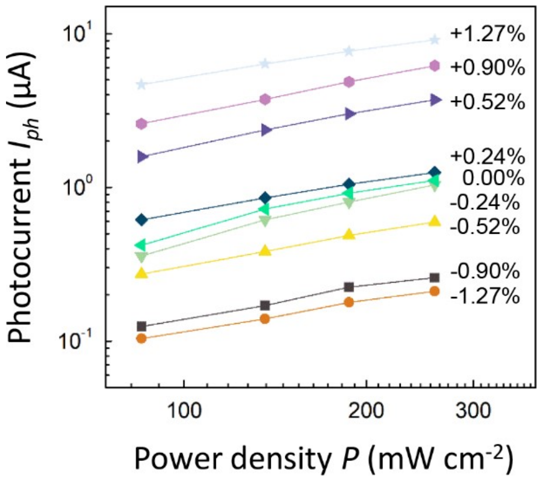

Fig. S10 Variations in the photocurrent I_{ph} with increasing P measured at +5 V for the MoS_2-monolayer-based photodetectors processed with various levels of in situ compressive and tensile strain ε_i.

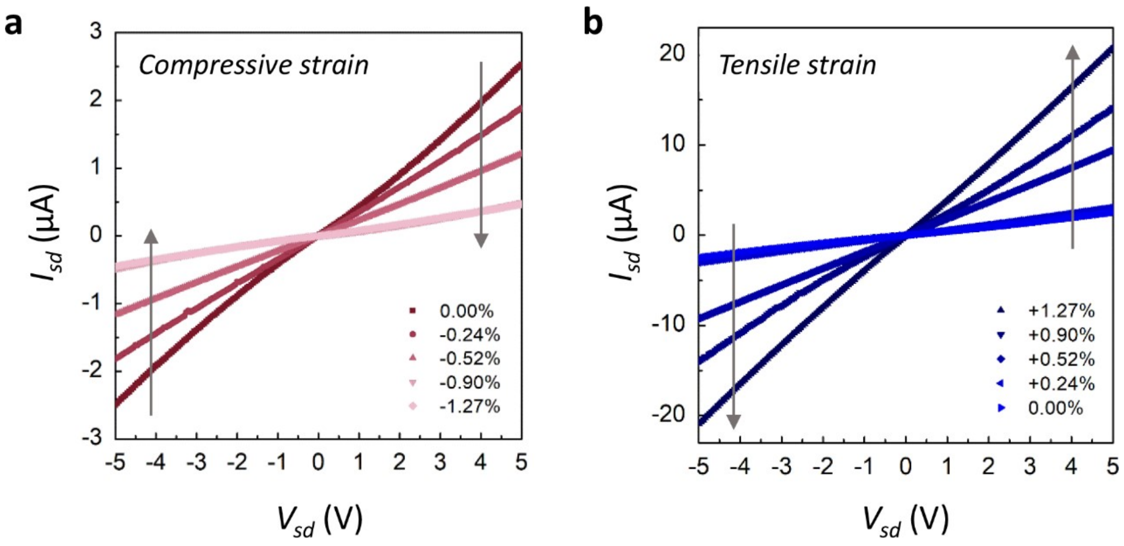

Fig. S11 I_{sd}–V_{sd} curves of the MoS_2-monolayer-based photodetectors processed with in situ (a) compressive and (b) tensile strain ε_i, which were measured at the laser power density P of 259 mW cm^{-2}.

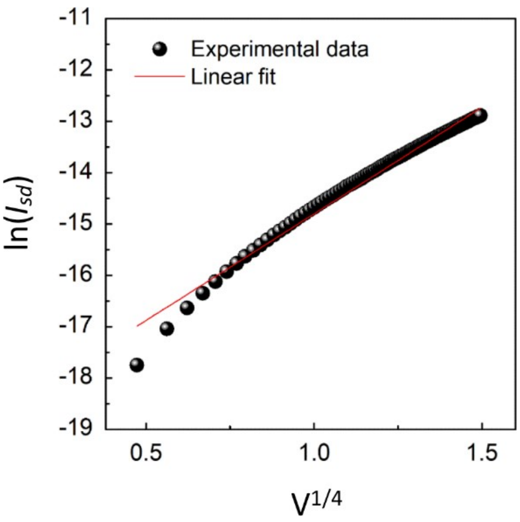

Fig. S12 Plot of $\ln(I_{sd})$ versus $V_{sd}^{1/4}$ for the MoS_2-based photodetector, indicating the conduction mechanism of the thermionic emission–diffusion, as assumed from the well-fitted line.

Table S1 Comparison of the response times of photodetectors based on MoS_2 monolayers; here, V_{sd} is the source–drain voltage, and V_g is the gate voltage.

Substrate	Method	Wavelength of the incident laser [nm]	V_{sd} [V]	V_g [V]	Rise time [s]/ Fall time [s]	Ref.
SiO_2/Si	CVD	532	1	100	3/500	1
SiO_2/Si	Exfoliation	561	8	-70	4/9	2
SiO_2/Si	Exfoliation	550	1	0	0.05/0.05	3
PI/PET	CVD	450	0.1–1	0	1.6/0.7	4
sapphire	CVD	532	0.5	0	36.7/56.9	5
SiO_2/Si	CVD	532	-	-	78/25	6
SiO_2/Si	CVD	365	1	0	2.04/6.64	7
PEN	CVD	white	1	0	30.9/24.8	8
PET	CVD	520	10	0	0.050/0.279	This work

(PI: polyimide, PET: polyethylene terephthalate, PEN: polyethylene naphthalate)

References cited in Table S1

[1] W. Zhang, J. Huang, C. Chen, Y. Chang, Y. Cheng, L. Li, *Adv. Mater.* **2013**, *25*, 3456.
[2] O. Lopez-Sanchez, D. Lembke, M. Kayci, A. Radenovic, A. Kis, *Nat. Nanotechnol.* **2013**, *8*, 497.
[3] Z. Yin, H. Li, H. Li, L. Jiang, Y. Shi, Y. Sun, G. Lu, Q. Zhang, X. Chen, H. Zhang, *ACS Nano* **2012**, *6*, 74.
[4] S. Pak, A. Jang, J. Lee, J. Hong, P. Giraud, S. Lee, Y. Cho, G. An, Y. Lee, H. S. Shin, S. M. Morris, S. Cha, J. I. Sohn, J. M. Kim, *Nanoscale* **2019**, *11*, 4726.
[5] Y. H. Zhou, H. N. An, C. Gao, Z. Q. Zheng, B. Wang, *Mater. Lett.* **2019**, *237*, 298.
[6] Y. Huang, F. Zhuge, J. Hou, L. Lv, P. Luo, N. Zhou, L. Gan, T. Zhai, *ACS Nano* **2018**, *12*, 4062.
[7] L. Zhao, K. Chen, F. Yang, M. Zheng, J. Guo, G. Gu, B. Zhang, H. Qin, G. Cheng, Z. Du, *Nano Energy* **2019**, *62*, 38.
[8] F. Li, T. Shen, L. Xu, C. Hu, J. Qi, *Adv. Electron. Mater.* **2019**, *5*, 1900803.

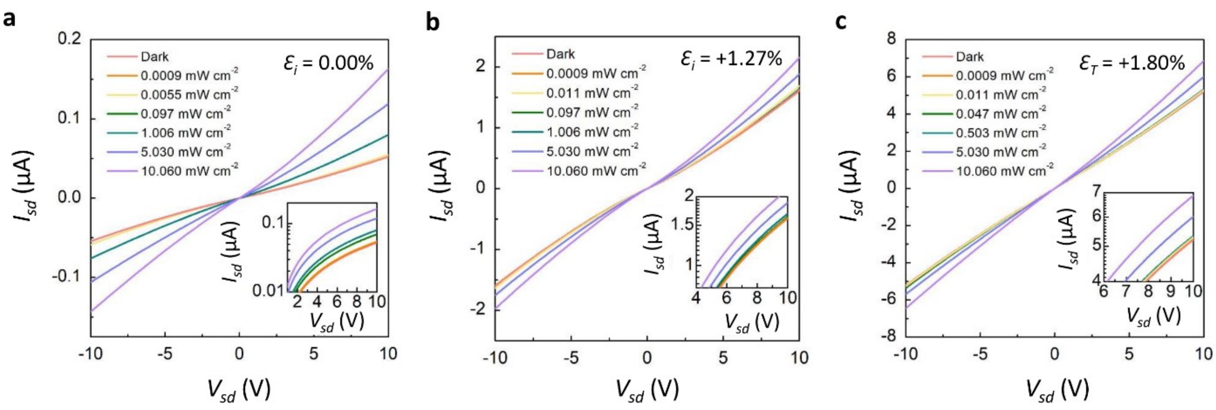

Fig. S13 I_{sd}–V_{sd} curves of the monolayer MoS_2 photodetectors processed with (a) no strain, (b) in situ strain of +1.27%, and (c) double strain of +1.80% at different power densities.

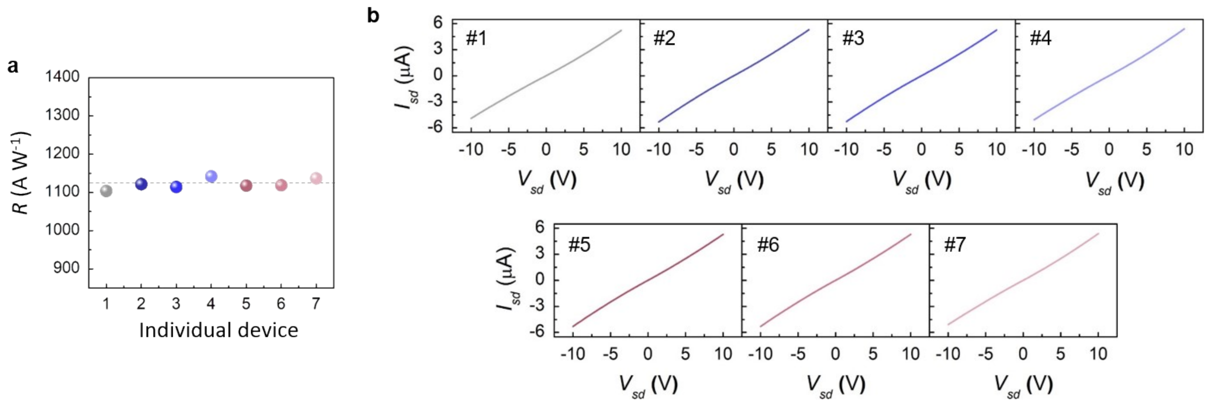

Fig. S14 (a) Plot of R values obtained by seven different measurements in the optimal conditions of applied strain and power density for monolayer MoS_2 photodetectors and (b) the corresponding individual I_{sd}-V_{sd} curves of the measurements.

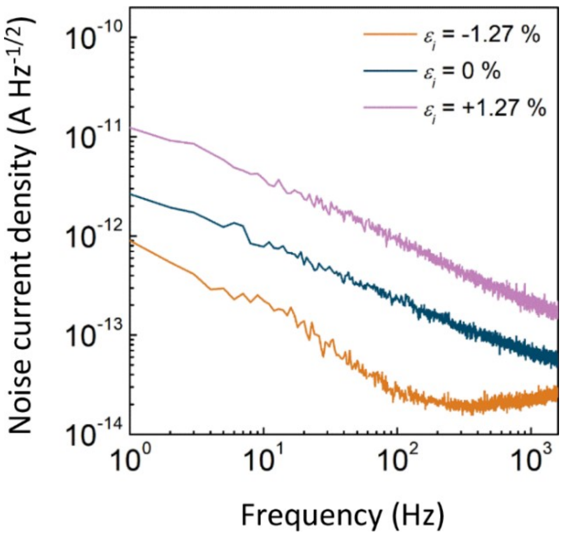

Fig. S15 Spectral noise current density as a function of frequency for the MoS_2 photodetectors processed with in situ strains of –1.27%, 0%, and +1.27%

Table S2. Reported detectivity D^* values in 2D material-based photodetectors, which was measured with the consideration of noise current.

Material	Substrate	Type of 2D materials (Thickness [nm])	Wavelength [nm]	Frequency [Hz]	Noise current [A Hz$^{-1/2}$]	D^* [Jones]	Ref.
MoS_2	SiO_2/Si	Monolayer (N/A)	635	N/A	~10^{-12}	7.7×10^{11}	1
$MoSe_2$		Nanosheet (N/A)		N/A	~10^{-9}	1.0×10^{11}	
$PdSe_2$	SiO_2/Si	Nanosheet (6)	1060	N/A	N/A	1.31×10^{9}	2
black-AsP	SiO_2/Si	Nanosheet (5~20)	~2300	N/A	~10^{-13}	~2.0×10^{8}	3
Te	Al_2O_3/Si	Nanosheet (18.8)	1700	1000	~10^{-10}	2×10^{9}	4
MoS_2/ WS_2	SiO_2/Si	Monolayer/ Monolayer (0.95/0.7)	405	N/A	~10^{-12}	7.17×10^{11}	5
MoS_2 (ε_i = 0.00%)	PET	Monolayer (~1)	532	1600	7.00×10^{-14}	8.9×10^{11}	*This work*
MoS_2 (ε_i = +1.27%)					2.05×10^{-13}	9.1×10^{12}	

* PET; polyethylene terephthalate

[1] D. Kufer, G. Konstantatos, *Nano Lett*. 2015, **15**, 7307.
[2] Q. Liang, Q. Wang, Q. Zhang, J. Wei, S. X. Lim, R. Zhu, J. Hu, W. Wei, C. Lee, C. Sow, W. Zhang, A. T. S. Wee, *Adv. Mater*. 2019, **31**, 1807609.
[3] M. Long, A. Gao, P. Wang, H. Xia, C. Ott, C. Pan, Y. Fu, E. Liu, X. Chen, W. Lu, T. Nilges, J. Xu, X. Wang, W. Hu, F. Miao, *Sci. Adv*. 2017, **3**, e1700589.
[4] M. Amani, C. Tan, G. Zhang, C. Zhao, J. Bullock, X. Song, H. Kim, V. R. Shrestha, Y. Gao, K. B. Crozier, M. Scott, A. Javey, *ACS Nano* 2018, **12**, 7253.
[5] C. Li, J. Zhu, W. Du, Y. Huang, H. Xu, Z. Zhai and G. Zou, *Nanoscale Res. Lett.*, 2021, **16**, 123.

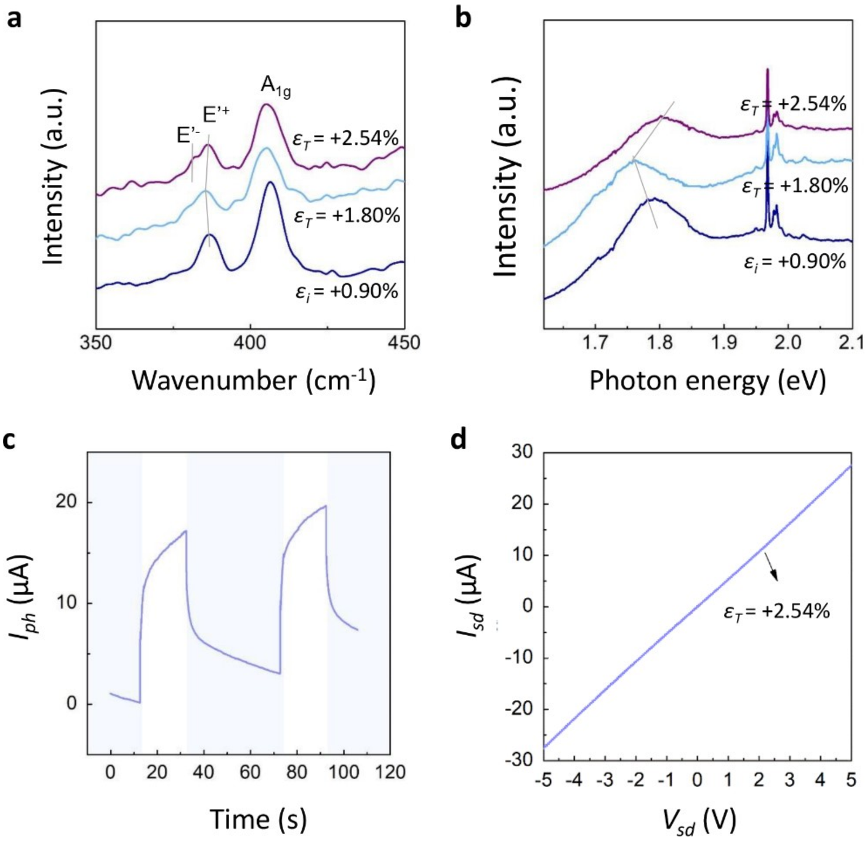

Fig. S16 Comparisons of the (a) Raman and (b) PL spectra of the double-strained MoS_2 films having the total strains of +2.54% and +1.80% with those of the in situ strained sample (ε_i ~ +0.9%), (c) the transient on/off switching behavior of the +2.54%-strained photodetector, and (d) the I_{sd}–V_{sd} curve of the +2.54%-strained photodetector.

Table S3 Performance comparison of visible-light photodetectors based on 2D materials with no applied gate voltage. Here, A is the active area, V_{sd} is the source–drain voltage, I_{ph} is the photocurrent, P is the light power density, and R is the photoresponsivity.

Material	Method	Type (Thickness [nm])	A [μm^2]	Substrate	Wavelength of the incident laser [nm]	V_{sd} [V]	I_{ph} [μA]	P [mW cm^{-2}]	R [A W^{-1}]	Ref.
MoS_2	Exfoliation	Monolayer (0.8)	5.46	SiO_2/Si	550	–7	0.0035	80 μW	0.001	55
$MoSe_2$	CVD	Monolayer (0.71)	446	SiO_2/Si	532	10	0.00181	100	0.013	56
$MoSe_2$	CVD	Monolayer (0.7)	-	SiO_2/Si	532,650	–1	0.0015	590	0.00026	57
WS_2	CVD	Monolayer (-)	-	SiO_2/Si	532	-	0.00012	-	0.0188	58
WS_2	CVD	Monolayer (0.8)	-	SiO_2/Si	500	1	0.045	0.2	3.07	59
WS_2	CVD	Monolayer (0.8)	25	SiO_2/Si	532	4	10	10	20	60
WSe_2	CVD	Monolayer (0.746)	100	SiO_2/Si	532	–1	0.03	25	1.1	61
$ReSe_2$	Exfoliation	Monolayer (0.66)	4	SiO_2/Si	633	–0.5	0.08	-	-	62
In_2Se_3	PVD	Monolayer (~1.2)	1.1	SiO_2/Si	532	–2	0.0045	0.026	340	63
GeS	Solution synthesis	Multilayer (160)	2	SiO_2/Si	405	3	0.0037	1.98	173	64
GeSe	PVD	Multilayer (15)	6	SiO_2/Si	633	–1.5	0.006	210.8	7.05	65
GeP	Exfoliation	Multilayer (4.3)	2.52	SiO_2/Si	532	–0.1	~0.001	0.32	3.11	66
SnS	CVD	Multilayer (25)	12.6	SiO_2/Si	532	–1	1.5	300	21.8	67
SnS_2	CVD	Multilayer (108)	75	mica	450	10	~0.04	1	2	68
SnSe	Sputtering	Multilayer (~15)	2000	SiO_2/Si	404	15	1.52	0.008	277.3	69
$SnSe_2$	CVD	Multilayer (3)	10	SiO_2/Si	530	3	1.3	6.38	1100	70
PbI_2	PVD	Multilayer (8.32)	-	PET	450	5	0.014	42.24	131.7	71
$CdS_xSe_{(1-x)}$	CVD	Multilayer (76)	36	mica	450	5	1.62	0.56	703	72
MoS_2 (ε_T = +1.80%)	CVD	Monolayer (1.06)	5000	PET	532	~10	~22.9	0.0009	1140	*This work*

(PET: polyethylene terephthalate, CVD: chemical vapor deposition, PVD: physical vapor deposition)

Table S4 Performance comparison of flexible photodetectors based on 2D materials. Here, V_{sd} is the source–drain voltage, *P* is the light power density, and *R* is the photoresponsivity.

Materials	Method	Type or thickness [nm]	Substrate	Wavelength of the incident laser [nm]	V_{sd} [V]	P [mW cm^{-2}]	R [A W^{-1}]	Bending cycles	Ref.
GaS	CVD	~3 layers	PET	254	2	0.5	19.2	-	73
GaSe	CVD	~5 layers	mica	white	10	3.27	0.03	-	74
GaTe	CVD	80	PET	473	5	3.36	0.03	200	75
InSe	Exfoliation	~12	PET	633	–10	~1	3.9	-	76
WSe_2	PLD	48	PI	635	10	0.0067	0.92	-	77
In_2Se_3	PLD	22.9	PI	532–635	–5	0.027	22.96	-	78
SnS	PLD	15	PI	370	5	0.03	115	100	79
Bi_2Se_3	PVD	~27	mica	735	0.1	26.7	0.0101	200	80
HfS_2/h-BN	CVD	Monolayer	PET	450	10	3.3	0.135	100	81
$Pb_{1-x}Sn_xSe$	CVD	15–45	mica	473	2	5.1	5.95	100	82
PbI_2	PVD	8.32	PET	450	5	42.24	147.6	100	71
SnTe	PVD	120	PET	635	1	~12 mW	49.03	80	83
Graphene/ MoS_2	CVD	Monolayer	PET	632.8	–0.1	0.645 µW	10	1000	84
V_2O_5/ MoS_2	Hydrothermal method	~4 layers	Al foil	554	1	4.1	0.0651	500	85
MoS_2	CVD	Monolayer	PET	532	–10	~5	9	-	86
MoS_2	CVD	Monolayer	PEN	405	–10 (V_g 80V)	5.73	0.02	1000	87
MoS_2	CVD	~6	PET	532	10	0.015 mW	0.0002	20	88
MoS_2 (ε_T = +1.80%)	CVD	Monolayer	PET	520–532	10	0.0009	1140	10000	*This work*

(PEN: polyethylene naphthalate, PET: polyethylene terephthalate, PI: polyimide, CVD: chemical vapor deposition, PLD: pulsed laser deposition, PVD: physical vapor depostion)